Ms Number : 4213 - Revision 1

Incorporation of Zn in the destabilization products of muscovite at 1175°C under disequilibrium conditions.

KARINE DEVINEAU[1,2,*], BERTRAND DEVOUARD[3,4,5], HUGUES LEROUX[6], LAURENT TISSANDIER[7]

[1] Université de Lorraine-ENSG, Laboratoire Environnement et Minéralurgie, UMR 7569, Vandoeuvre-les-Nancy, F-54500, France

[2] CNRS, Laboratoire Environnement et Minéralurgie, UMR 7569, Vandoeuvre-les-Nancy, F-54500, France

[3] Clermont Université, Université Blaise Pascal, Laboratoire Magmas et Volcans, BP 10448, F-63000 Clermont-Ferrand, France

[5] CNRS, UMR 6524, LMV, F-63038 Clermont-Ferrand, France

[5] IRD, R 163, LMV, F-63038 Clermont-Ferrand, France

[6] Unité Matériaux et Transformations, CNRS UMR 8207, Université Lille 1, 59655 Villeneuve d'Ascq, France

[7] Centre de Recherches Pétrographiques et Géochimiques, CNRS-Université de Lorraine, 15 rue Notre-Dame des Pauvres, 54501 Vandoeuvre-les-Nancy, France

[*] E-mail: karine.devineau@univ-lorraine.fr

ABSTRACT

This work reports on the thermal decomposition of muscovite within a granite powder doped with 8.5 wt% ZnO and heated during 10 min to 68 h at 1175°C. Samples were characterized

using analytical scanning and transmission electron microscopy. After 10 min, muscovite is completely pseudomorphosed by Si-rich glass, spinel structure phases, and minor mullite. Spinel phases incorporate Zn, but their compositions depend on their position within the muscovite pseudomorphs. Al-rich oxides crystallize at the core of the pseudomorphs while Zn-Al spinels are located at the rims. The most Al-rich spinels have compositions close to γ-Al_2O_3, a metastable transition alumina, with up to 5 wt% MgO, 2 wt% Fe_2O_3, 4 wt% ZnO, and 9 wt% SiO_2. The most Zn-rich spinels show compositions intermediate between Al_2O_3 and gahnite ($ZnAl_2O_4$), with up to 31 wt% ZnO and significant contents of MgO (3 wt%), Fe_2O_3 (5 wt%), and SiO_2 (10 wt%). After 68 h, stable spinels are gahnite close to the end-member composition with MgO and Fe_2O_3 contents below ca. 5 wt%, and SiO_2 contents ca. 1 wt%. These results support the existence of a metastable solid solution between γ-Al_2O_3 and gahnite. This experimental work shows that Zn can be incorporated in spinel structures after heating at 1175°C during short durations and Zn is preferentially incorporated in the muscovite pseudomorphs as opposed to the Qtz-Fds glass. Consequently, the thermal breakdown of phyllosilicates can be a viable process to immobilize heavy metals such as Zn.

Keywords: Crystal growth, Al-Zn oxide, gahnite, high-*T* studies, experimental petrology, muscovite, focused ion beam, electron diffraction, electron microscopy.

INTRODUCTION

Deposition of heavy metals contaminated wastes (e.g., sewage sludge, tannery sludge, steelworks slags, dredged harbour sediments, waste incinerator ashes, *etc.*) can be helped by immobilization of these heavy metals as constituents of mineral phases. The use of contaminated wastes as secondary raw materials incorporated to quartz-feldspar-clay mixtures in ceramics is a useful way to immobilize heavy metals (e.g., Bruhns and Fischer 2001;

Basegio et al. 2002; Hamer and Karius 2002; Cusido et al. 2003; Ferreira et al. 2003; Jordan et al. 2005; Merino et al. 2007; Montero et al. 2009; Reinosa et al. 2010; Donald 2010; Haiying et al. 2011).

On the other hand, weathered granites are potentially important starting products for the elaboration of traditional ceramics (floor tiles, sanitaries…) since their main minerals, i.e., quartz, feldspars, and phyllosilicates, constitute the main raw materials for the production of these ceramics (e.g., Monteiro et al. 2004; Menezes et al. 2005; Vieira and Monteiro 2006; Torres et al. 2007; Hojamberdiev et al. 2011). To evaluate the feasibility of using weathered granites as starting materials in the ceramic industry, previous studies dealt with the mineralogical, chemical, and textural evolutions of weathered granite powder heat-treated at 1175°C and room pressure (1 bar), the usual conditions in ceramic works. Two main reaction mechanisms have been observed: i) partial melting and reactions involving quartz and feldspars (Devineau et al. 2005) and ii) the breakdown of muscovite (Devineau et al. 2006, 2007). This experimental study shows that muscovite is completely transformed at 1175°C after 5 min. Muscovite pseudomorphs consist of glass, γ-Al_2O_3, and mullite. γ-Al_2O_3 is described as the first destabilization product of muscovite at high-*T* (Roy 1949; Sundius and Byström 1953; Brindley and Maroney 1960; Eberhart 1963; Brindley and Lemaître 1987; Devineau et al. 2006). This metastable alumina phase forms under strong disequilibrium conditions for heating durations of muscovite of 5 to 40 min at 1175°C. γ-Al_2O_3 has a lacunar spinel structure which can accommodate substituting elements up to at least 10 wt% SiO_2, 4-8 wt% FeO_{tot}, and a few weight percents of MgO (Devineau et al. 2006 and references therein).

Spinel group minerals are good candidates to incorporate heavy metals in their structure, and thus potential storage phases for those pollutants. Naturally occurring spinel end-members include gahnite ($ZnAl_2O_4$), franckIinite ($ZnFe_2O_4$), trevorite ($NiFe_2O_4$), chromite, cochromite, magnesiochromite, manganochromite, and zincochromite ($FeCr_2O_4$,

$CoCr_2O_4$, $MgCr_2O_4$, $MnCr_2O_4$, and $ZnCr_2O_4$, respectively), coulsonite, magnesiocoulsonite, and vuorelainenite (FeV_2O_4, MgV_2O_4, and MnV_2O_4), cuprospinel ($CuFe_2O_4$). Numerous and extensive solid solutions are known to occur between these end-members. In addition, $NiCr_2O_4$ ("nichromite") and synthetic cadmium ferrite, nickel aluminate, and copper aluminate spinels are stable structures (Tellefsen et al. 1984; Shih et al. 2006; Shih and Leckie 2007; Hu et al. 2010).

This work focuses on the incorporation of ZnO in the mineral products of muscovite decomposition for the following reasons: i) Zn is an ubiquitous heavy metal in waste incinerator ashes (Cheeseman et al. 2003; Park et al. 2003; Favoni et al. 2005; Haiying et al. 2011), sludge wastes from water treatment plant (Jordan et al. 2005; Garcia-Valles et al. 2007; Montero et al. 2009), galvanic sludges (Magalhães et al. 2004a, 2004b; Silva and Mello-Castanho 2004; Magalhães et al. 2005; Silva and Mello-Castanho 2007; Silva et al. 2008; Reinosa et al. 2010; Silva et al. 2010), dewatered sewage sludges (Kanchanapiya et al. 2006), dredged harbour sediments (Hamer et al. 2002), steelworks slags (Favoni et al. 2005), and tannery sludges (Basegio et al. 2002); and ii) the spinel structure can immobilize Zn in a stable zincian spinel phase (gahnite). The aim is to determine if short duration heat-treatments, as those used in manufacturing ceramics, are sufficient for Zn to be incorporated in the structure of the destabilization phases of muscovite. The present study addresses this question with an experimental study of the mineral assemblages produced during the early stages of muscovite decomposition. This kinetic study documents the reaction paths toward equilibrium which would have been much more difficult to unravel with currently used industrial mixtures. Based on previous studies (Devineau et al. 2005, 2006, 2007), heating durations of 10 min, 40 min, and 68 h at 1175°C were chosen in order to investigate disequilibrium and equilibrium assemblages.

STARTING MATERIAL

The starting material is a leucogranite from the Margeride pluton, French Massif Central. Leucogranites, aplites and pegmatites occur as dykes, sills or small stocks crosscutting the main Hercynian granite body (Pichavant and Manning 1984, see their Fig. 1). The sample chosen was collected in the Entraygues region, near the "Grangette" locality. It is a fine-grained (ca. 0.5 mm), aplitic leucogranite, slightly weathered as indicated by its yellowish-pinkish color. The modal composition is quartz (36%), albite (21%), orthoclase (33%), and muscovite (10%). The leucogranite also contains accessory tourmaline and minor clay minerals (montmorillonite, kaolinite). Chemical analyses of the bulk leucogranite and main minerals (albite, muscovite and K-feldspar) are given in Devineau et al. (2005).

EXPERIMENTAL METHODS

Experimental procedure

The Grangette leucogranite was powdered to grain sizes ranging from < 3 to about 200 μm, with ca. 50% of particles being < 30 μm. The granitic powder was then doped with 8.5 wt% ZnO powder (particle size < 1 μm, Sigma-Aldrich®), mixed with water, and this wet mixing was cold-pressed under pressures up to 74 MPa into a cylindrical shape (height: 12 mm, diameter: 13 mm). Residual porosity of dried cylinders was estimated to 25%, based on specific gravity. The one-atmosphere vertical furnace (GERO HTRV 70-250) was first equilibrated at 1175°C. Specimens were then placed in a platinum crucible (height: 20 mm, external diameter: 20 mm) and suspended in a platinum "wire basket" close to the extremity of a ceramic rod introduced in the hot zone of the furnace. The tip of an S-type thermocouple (Pt/PtRh10), placed on the ceramic rod, was located 1 cm above the crucible. This thermocouple was previously calibrated against the melting points of gold (1064°C) and palladium (1554°C), and controlled the temperature during the experiments with an accuracy

of ±2°C. Heat-treatment experiments were carried out in air (P=1 bar) for run durations of 10, 40 min, and 68 h. At the end of the experiments, samples were removed from the furnace and quenched in air.

The residual porosity and the consistency of the results allows us to be confident that the experimental *T* has been reached throughout the whole sample even for the shorter run durations. The cooling time is not known with precision, but is estimated to a few minutes. It must be noted that no texture of rapid growth have been observed in the samples that could be attributed to cooling effects. The lack of textural difference between the core and the rim of the samples also suggests a cooling fast enough to quench the mineral reactions.

Analytical methods

Major-element and Zn concentrations of untreated and heat-treated samples were measured by inductively-coupled plasma atomic emission spectroscopy (ICP-AES) and atomic absorption, respectively (Service d'Analyse des Roches et des Minéraux (SARM) - Centre de Recherches Pétrographiques et Géochimiques (CRPG) - Nancy). The adsorbed water (H_2O^-) content was measured by weighing the sample before and after heating at 100°C during 24h. The structural water (H_2O^+) was measured as the weigh difference between the sample dried at 100°C and the sample heated at 1000°C during 3h. Relative uncertainties based on reproducibility are better than 1% for SiO_2 and Al_2O_3, 5% for Fe_2O_3, Na_2O, and K_2O, 10% for MgO, CaO, MnO, and TiO_2, 20% for P_2O_5, and < 3% for Zn.

Petrographic thin sections were examined by transmitted and reflected-light microscopy and by scanning electron microscopy (SEM) using backscattered electron (BSE) imaging on a Hitachi FEG S4800 microscope (Université de Lorraine, Nancy, France) operated at 5 or 15 kV accelerating voltage. Microanalyses were acquired on the SEM with a ThermoNORAN

150 energy-dispersive X-ray spectrometer equipped with a Si(Li) detector and SAMx
151 microanalysis software.

152 Major-element and Zn analyses of minerals and glasses were obtained by electron probe
153 microanalysis (EPMA) using a Cameca SX50 microprobe (University de Lorraine, Nancy,
154 France). Operating conditions were 15 kV accelerating voltage, 10 nA beam current and 10 s
155 counting time on peak. Natural and synthetic standards were used and the PAP program
156 (Pouchou and Pichoir 1991) was applied for data correction.

157 In order to investigate the nanometric reaction phases in the muscovite pseudomorphs,
158 focused ion beam (FIB) was used to prepare electron-transparent foils for transmission
159 electron microscopy (TEM) and scanning transmission electron microscopy (STEM)
160 observations. Five representative regions of interest were selected in muscovite
161 pseudomorphs after SEM observation. FIB cuts were prepared with a dual-beam FEI Strata
162 DB 235 FIB-FESEM (IEMN, Lille, France). The resulting TEM-foils were ca. 15-20 μm by
163 10-15 μm and 100 nm thick (for technical details, see, e.g., Overwijk et al. 1993; Wirth 2004;
164 Leroux et al. 2008). The transfer of the sections to a TEM Cu-grid support was performed
165 using a micromanipulator. The main steps of the FIB sample preparation process are
166 illustrated in Leroux et al. (2008; see their Fig. 2).

167 The TEM study was performed with a FEI Tecnai G2 20 (electron microscopy facility,
168 Lille, France), fitted with a LaB_6 filament and operated at 200 kV. Microstructures were
169 studied by direct TEM imaging (bright field) or in the STEM mode (bright and dark field).
170 Crystal structures were determined with selected-area electron diffraction (SAED) patterns.
171 Microchemical analyses were obtained with the Si(Li) diode (EDAX) EDS detector attached
172 to the TEM. Analyses were obtained in STEM mode from selected zones. Spectral mapping
173 was applied to regions of special interest up to 4 x 5 μm, with drift compensation. Spectral
174 maps were post-processed to extract quantitative analyses or profiles from selected regions.

Data were processed with the ES-Vision software. Absorption and element-specific yields (k-factor) corrections were applied to obtain quantitative elemental compositions. Laboratory k-factors were experimentally determined using the parameterless method of Van Cappellen (1990) with silicate standards. For absorption correction, thicknesses were fixed to 100 nm, which appeared an accurate estimate for the FIB sections.

RESULTS

This paper focuses on the thermal breakdown of muscovite within a quartz-feldspar matrix doped with ZnO powder. The mineralogical evolution of the quartz-feldspar matrix displays the same behavior as the Zn-free quartz-feldspar matrix studied in Devineau et al. (2005). The main results are summarized below. During partial melting at 1175°C, quartz and feldspars progressively decrease in abundance; the amount of melt produced increases sharply after 40 min and leads to a strong decrease of the porosity of the powder. After 68 h of heat-treatment, the porosity has largely disappeared and glass extends all over, leaving only minor trapped porosity. Original alkali feldspars of the granitic powder begin to melt after 5 min, and almost disappear in samples reacted for 40 min. For 68 h durations, all feldspars are melted in the glass phase and only residual quartz persists. Newly formed K-feldspars are transitionally observed in the matrix for the short-duration experiments (10 and 40 min). The only difference between the current study using Zn-doped granite powder and the experiments described in Devineau et al. (2005) is the presence of Zn-rich grains (willemite and unreacted zincite) inside the partially molten quartz-feldspar matrix.

In this paper, textural results from SEM and TEM imaging will be presented first, with minimal information from microanalysis, and the quantitative chemical analyses (bulk, microprobe, and TEM-EDS) will be addressed in a later section.

199

200 **Scanning Electron Microscopy**

201 BSE imaging of the pressed pellets before heating (Fig. 1) shows the heterogeneous
202 distribution of ZnO powder aggregates. BSE imaging of heated samples for the different run
203 durations shows pseudomorphs of former muscovite grains within a melt produced by the
204 partial melting of quartz-feldspars assemblages and relict quartz (Fig. 2 and Supplemental
205 Figure A1[1]). Even for the shorter duration, no relics of unreacted muscovite can be recognized
206 within the pseudomorphs. A characteristic feature of these muscovite pseudomorphs is the
207 presence of bubbles (Figs. 2a and 2c) which have been discussed specifically by Devineau et
208 al. (2007).

209 For the short duration runs (10 and 40 min), muscovite pseudomorphs display newly-
210 formed crystallites disposed in parallel alignments, outlining the cleavage directions of the
211 former muscovites, except in the vicinity of bubbles where they are deviated. Some elongated
212 crystallites are not parallel to the former cleavages and display an orientation roughly at 120°.
213 In the core of the pseudomorphs, the crystallites are submicrometric and their sizes are
214 difficult to determine precisely at the SEM scale (ca. 50 nm and up to ca. 600 nm in the
215 longer direction). Muscovite pseudomorphs are systematically outlined by coarser oxides with
216 a brighter BSE contrast (Figs 2b and 2d). Crystallites in these rims have similar morphologies
217 and orientation, but are somewhat thicker (up to 70 x 500 nm at 10 min and 200 x 1000 nm at
218 40 min) and EDS reveals they are enriched in Zn. There is a progressive variation of the size
219 and BSE contrast of the crystallites from rim to core. For the 68 h runs, pseudomorphs usually
220 do not display differences of texture from rim to core but a homogeneous texture of well
221 individualized Zn-Al oxides within a homogeneous Si-Al-rich phase. Crystallites are coarser

[1] Deposit item AM-YR-XXX, Supplementary figures and tables. Deposit items are available two ways: For a paper copy contact the Business Office of the Mineralogical Society of America (see inside front cover of recent issue) for price information. For an electronic copy visit the MSA web site at http://www.minsocam.org, go to the *American Mineralogist* Contents, find the table of contents for the specific volume/issue wanted, and then click on the deposit link there.

(ca. 0.3 x 1.3 μm) and less elongated than in the short duration runs. However, the largest pseudomorphs (up to 300 μm; Fig. 2e) display core-rim differences. The rim texture is similar to smaller pseudomorphs, but the core retains a texture similar to what was observed in the rims for the short duration runs, with mostly oriented elongated oxides ca. 80 x 900 nm.

The textures described above are best observed in lateral sections of the former muscovite crystals. Basal sections also display core-rim differences, but the textures in the cores display complex heterogeneous mixtures of oxides (Supplemental Figure A1[1]) with small crystallites ca. 50 to 300 nm, elongated crystals (50-100 nm x 2-3 μm) and hollow, euhedral crystals (0.5 x 1 μm).

Transmission Electron Microscopy

FIB cuts. In order to characterize the nano- to micrometer-sized reaction products in muscovite pseudomorphs, FIB cuts were carried out on lateral sections, parallel and perpendicularly to the direction of the former muscovite cleavages (longitudinal and transversal sections, respectively), in two crystals selected from the optical and SEM observations (see FIB cut craters on Figs 2a and 2e and details on Supplemental Figure A2[1]). For muscovite heated during 10 min (first reaction products), the longitudinal FIB cut was carried out in the core region of the pseudomorph (Supplemental Figure A2a[1]) but close to the rim (ca. 5 micrometers away from the edge of the pseudomorph). The transversal foil was cut across the rim and several micrometers into the core (Supplemental Figure A2b[1]). For the 68 h duration, a first longitudinal FIB cut was extracted in a homogenous region representative of most pseudomorphs. A second longitudinal cut and a transversal cut were made in a large pseudomorph to study the transition between the coarser grained rim and the finer-grained core (Supplemental Figure A2c[1]).

TEM Imaging and SAED. Figures 3a, 5a, 6a, 6d, and 7a show general views of the FIB TEM foils at low-magnification. All slices display crystals embedded in a Si-Al-rich glass phase. Large scale, parallel striations observed on these figures are artifacts from the FIB cutting, and in no way structures inherited from the former muscovite.

In the 10 min sample, the longitudinal cut (Fig. 3a) displays an homogeneous texture. Irregularly shaped crystals with a mottled contrast (Figs. 3b and 3c), from a few tens of nm up to ca. 0.6 x 1.2 μm, occur along with elongated crystals, ca. 20 x 300 nm, roughly oriented at 120° along three directions (Fig. 3b). EDS analyses of both elongated and irregular crystals indicate Zn-Al oxides (see compositions below). SAED patterns of large irregularly shaped crystals, obtained from two different orientations, can be indexed as a spinel structure (Fig. 3d). SAED patterns were also recorded using a large selection aperture in order to get diffraction patterns from a large number of crystals in various orientations from an area covering about the full width of the TEM foil (selection area diameter = 6 μm). From this SAED pattern showing diffraction rings (Fig. 4a), integrated radial intensities were extracted in order to obtain a diffraction profile similar to what could be obtained from powder diffraction data (Fig. 4b). All d_{hkl} values in this profile closely match the values expected for a spinel structure (Fig. 4c), and no extra peaks could be identified. Still in the 10 min sample, the transversal cut (Fig. 5a) shows elongated, parallel crystals, 10-80 nm in width and up to 1000 nm in length, with some outliers oriented at an angle from the general direction of elongation (Fig. 5b), as well as a minor amount of shorter crystals. All those crystals have similar aspects and frequently display mottled contrasts (Figs. 5b and 5c). SAED patterns, recorded from the largest available crystals in two different orientations, can be indexed as a spinel structure (Fig. 5e). As for the longitudinal cut, ring SAED patterns were recorded from crystals in various orientations. The diffraction ring patterns display similar d-spacings but different intensities from those recorded in the longitudinal cut (shown on Fig. 4). Crystals in

the rim and core regions of the pseudomorph, however, differ in two ways: i) most crystals situated near the edge of the pseudomorph are ca. 70 nm wide (Fig. 5c), whereas crystals in the core region have widths that range from ca. 10 to 70 nm (Fig. 5b), maximal widths and lengths being similar in both regions, however; and ii) EDS analyses indicate that crystals near the rim are Zn-Al oxides, whereas crystals in the core region are Al oxides with a composition close to alumina (see analyses below). In addition, rare crystals display a different morphology, euhedral, frequently skeletal, up to 390 nm, and with sharp diffraction contrast (Figs. 5d and 5a, arrowed). Diffraction patterns and EDS analyses of these euhedral crystals are characteristic of mullite (Fig. 5f). Finally, some matrix of quartz-feldspar glass and relict quartz can be observed on one side of the section (Fig. 5a). At the limit between the matrix and the pseudomorph, some crystals of willemite (as determined by EDS) display euhedral, hexagonal shapes (Figs. 5a and 5c).

In the 68h sample, the longitudinal cut carried out in the homogenous region (representative of most pseudomorphs) show only large crystals, ca. 0.7 x 1 μm, with peculiar subhedral morphologies (Figs. 6a and 6b). EDS analyses and SAED patterns (Fig. 6c) indicate gahnite. The second longitudinal cut shows two regions with distinct textures (Fig. 6d). The external region, cut within the homogeneous, coarse grained rim, show large gahnite crystals identical to what was observed in the first longitudinal section. The core region contains both large irregular crystals ca. 0.3 x 0.5 μm and elongated crystals ca. 42 x 700 nm in a texture similar to what was observed in the longitudinal section of the 10 min sample (Figs. 3a and 3b). Compared to Figure 3c, the large crystals at 68 h (Figs. 6a and 6b) have larger average sizes, mottled contrast less pronounced and, although still irregular, their outlines tend to be subhedral. The transversal section (Fig. 7) also shows two regions, an external one with the same texture of large gahnites as observed in the homogeneous longitudinal cut, and a core

295 region with euhedral elongated gahnite crystals ca. 0.05 x 1 μm. The texture in the core region
296 resembles the one observed in the transversal cut of the 10 min sample (Fig. 5).
297
298 **Chemical compositions**
299 **Bulk compositions.** Bulk chemical compositions of the untreated and heat-treated
300 samples are given in Table 1. The analyses show a progressive decrease in ZnO from 8.52
301 wt% before heat-treatment to 7.43 wt% after 68 h. 5000 ppm Zn are lost in the first 10 min.
302 Zn is lost by volatilization because the point boiling of Zn is 917°C (Lide 2008). It went to the
303 gas phase in the oven (in other HT experiments with Zn, we could observe that it recondensed
304 on the cooler parts of the ceramic rod). Zn is partially lost within the first minutes of heating
305 because for longer durations, as the melting reactions become important, Zn gets dissolved in
306 the melt. Adsorbed water (H_2O^-) is lost before 10 min. Structural water decreases from 0.82 to
307 0.27 wt% in 10 min but no further loss is observed between 10 min and 68 h. Concentrations
308 for all other elements, including Na and K, are constant within analytical errors.
309 **Evolution of muscovite-pseudomorphs and quartz-feldspar glasses compositions.**
310 EPMA analyses of unheated muscovite, muscovite pseudomorphs, and quartz-feldspar glass
311 around the pseudomorphs are reported in Table 2.
312 Quartz-feldspar glasses adjacent to the TEM foils prepared in the pseudomorphs were
313 analyzed by EPMA. The average compositions are similar. However, Devineau et al. (2005)
314 observed that glass compositions are highly variable after 10 min heating but are reasonably
315 homogeneous after 68 h (except in the vicinity of melting quartz grains). The glass measured
316 in the 10 min sample contains 5.2 wt% ZnO. The glass at 68 h sample contains 3.6 wt% ZnO.
317 These values should be taken with care, however, the glass containing numerous
318 submicrometer crystals rich in ZnO (unreacted ZnO and willemite).

Analyses of muscovite pseudomorphs in Table 2 correspond to bulk compositions (crystallites and glass). For short durations, the Zn-enriched rims are too small to be analyzed properly by EPMA; bulk compositions for this region were recalculated from STEM spectral mapping (see below). For the 68 h sample, two values were obtained by averaging analyses: one composition corresponding to the homogeneous texture that is the most frequent for pseudomorphs at 68 h, and another corresponding to the finer-grained core region of the large pseudomorph described above (Fig. 2f). Bulk compositions of muscovite pseudomorphs show a progressive decrease in K_2O (from 11 to 4 wt%) and increase in Na_2O (from 0.6 to 3 wt%) relative to the starting muscovite (Table 2), as was observed and discussed in Devineau et al. (2006). The summation increases from 95 to more than 98 wt%, due to water loss. After 10 min heating, the core of the muscovite pseudomorphs contain 0.2 wt% ZnO (1900 ppm Zn), well above the detection limit (350 ppm Zn). The transversal TEM cut through the thin Zn-enriched rim (Fig. 5a) was mapped using STEM with a spatial resolution of 14 nm (Figs. 8a and Supplemental Figure A3[1]). A quantitative profile was reconstructed from the spectral map (Fig. 8b). Zn concentrations decrease steeply from 16 wt% at the edge of the pseudomorph down to 0.5 wt% ZnO at a distance of 3.5 μm from the edge. The small but significant difference between this value and the one measured by microprobe (0.2 wt%) can be attributed to the lack of representativity of the 4 x 5 x 0.1 μm region analyzed by STEM. For the 68 h run, EPMA analyses indicate that the pseudomorphs with a homogeneous texture have average ZnO contents of 17 wt%. In the largest pseudomorphs, however, a finer-grained core is visible. In the large pseudomorph studied (Fig. 2f), the average Zn content decreases continuously from the edge of the pseudomorph to the core, down to a minimum of 13 wt% ZnO at 20 μm from the edge.

Reaction phases in muscovite pseudomorphs. Submicrometric reaction phases in muscovite pseudomorphs were analyzed by TEM-EDS. Despite the high lateral spatial

344 resolution of TEM microanalyses (<10 nm), analyses can be contaminated by the surrounding
345 glass when crystals are thinner than the 100 nm thick TEM foil. Special attention was paid to
346 avoid such crystallites (see discussion). Table 3 summarizes the average compositions of
347 crystallites and glass within muscovite pseudomorphs. Total iron is reported as Fe_2O_3 because
348 ferric iron is expected for these high-temperature experiments performed in air.

349 In the 10 min sample, Zn-Al oxides show a range of compositions from Al-rich oxides
350 to Al-Zn oxides. All these oxides have a spinel structure, as determined from electron
351 diffraction. Average composition of the most Al-rich oxides (Table 3) is close to Al_2O_3. γ-
352 Al_2O_3 is a transition alumina with a spinel structure and it has frequently been reported in
353 similar experiments (Roy 1949; Sundius and Byström 1953; Eberhart 1963; Brindley and
354 Lemaître 1987; MacKenzie et al. 1987; Otero Arean et al. 1997; Barlow and Manning, 1999;
355 Devineau et al. 2006; Shih and Leckie 2007). This phase shows, however, important
356 deviations from the alumina end-member (Table 3), with significant contents of MgO (5
357 wt%), Fe_2O_3 (2 wt%), but also SiO_2 (9 wt%). The most Zn-rich Al-Zn oxides (Table 3) show
358 a composition intermediate between Al_2O_3 and gahnite, with 31 wt% ZnO, and significant
359 contents of MgO (3 wt%), Fe_2O_3 (5 wt%), and SiO_2 (10 wt%). Intermediate compositions are
360 plotted on a SiO_2-Al_2O_3-ZnO diagram in Figure 9. In a ZnO vs. Al_2O_3 diagram (Supplemental
361 Figure A4[1]), these intermediate compositions show a clear negative correlation. Average
362 analysis of glass within the pseudomorphs is also reported in Table 3. Individual glass
363 analyses (Fig. 9) show a range of Si/Al wt. ratio between 1.8 and 3. Glasses are systematically
364 poor in Zn, with ZnO contents around 0.4 wt%, close to the estimated detection limit. Mullite,
365 with a molar ratio of $(Al+Fe^{3+})/Si = 3.9$ (Table 3; Fig. 9), closely matches the stoichiometry
366 of the aluminous member of the mullite solid solution ($2Al_2O_3 \cdot SiO_2$). One willemite grain
367 located in the partially molten quartz-feldspar matrix between quartz and the surface of

368 muscovite pseudomorphs was also analyzed by TEM-EDS. This analysis is close to the
369 expected stoichiometry (Table 3).

370 After 68 h heating, gahnite analyses are stoichiometric and close to the end-member
371 composition (Table 3; Fig. 9). MgO and Fe_2O_3 contents sum up to ca. 5 wt%, but the SiO_2
372 content is only 1 wt%. Average analyses of glasses are characterized by an increase in SiO_2
373 (from 68 to 73 wt%) and ZnO (from 0.4 to 1.8 wt%; Table 3). Individual analyses of glass
374 show less variability than at 10 min (Fig. 9).
375
376 **DISCUSSION**
377 **Muscovite destabilization phases**
378 Destabilization products observed in muscovite pseudomorphs are spinel phases, Si-Al-
379 rich glass, and minor mullite.
380 Al-rich phases with a spinel structure and compositions ranging from nearly pure
381 alumina (4 wt% ZnO) to Al-Zn oxides up to 36 wt% ZnO, are unambiguously determined by
382 SAED and EDS. SAED ring patterns recorded from large areas show a perfect match with
383 powder diffraction data for spinel structures, independently of the Zn content. The difference
384 in cell parameter between γ-Al_2O_3 (a = 7.91 Å; experimental value from Guttiérez et al. 2001)
385 and gahnite (a = 8.09 Å; ICDD PDF file #5-669) is only 2%, within the error of SAED.
386 Differences in intensities between SAED ring patterns recorded in the transversal and
387 longitudinal cuts at 10 min can be explained by different preferential orientation of the
388 crystallites.
389 γ-Al_2O_3, a transition alumina with a spinel structure, has frequently been reported in
390 similar experiments (Roy 1949; Sundius and Byström 1953; Eberhart 1963; Brindley and
391 Lemaître 1987; MacKenzie et al. 1987; Otero Arean et al. 1997; Barlow and Manning 1999;
392 Devineau et al. 2006; Shih and Leckie 2007). γ-Al_2O_3 is generally interpreted as a defect

spinel with a formula $Al_{8/3}\,\square_{1/3}\,O_4$ ($\square$=vacancy) after reformulation on the basis of 4 oxygens. The distribution of the 1/3 vacancies per formula unit between the tetrahedral and octahedral sites of the spinel structure can be either fully ordered in one or the other site, or disordered (see Guttiérez et al. 2001 for a discussion). In this study, we evidence a solid solution from γ-Al_2O_3 to compositions close to the gahnite end member, that can be described by an $Al_{2/3} + \square_{1/3} = Zn$ substitution and a general formula of $Zn_x\,Al_{(8-2x)/3}\,\square_{(1-x)/3}\,O_4$. Considering also minor divalent and trivalent substituents for Zn and Al, respectively, and a formula of $M^{2+}_x\,M^{3+}_{(8-2x)/3}\,\square_{(1-x)/3}\,O_4$, our analyses from muscovite pseudomorphs are characterized by x values ranging continuously from 0.25 to 0.76 (at 10 min) and x = 0.91 at 68 h. These values are calculated from the average analyses of Al-rich spinel (γ-Al_2O_3), Zn-rich Al-Zn spinel, and gahnite reported in Table 3, respectively (note that to obtain the x value, Al-rich spinel must be recalculated on the basis of 4 oxygens, whereas it is calculated on the basis of 3 oxygens in Table 3 in order to evidence its Al_2O_3 stoichiometry). This suggests that the γ-Al_2O_3 - $ZnAl_2O_4$ solid solution is extensive and probably continuous. Hansson et al. (2004) experimentally studied the Al_2O_3-ZnO phase diagram in air, and showed that an extensive spinel solid solution between gahnite and Al_2O_3 is stable only for temperatures above 1500 °C. In this study we show that such intermediate compounds can be formed metastably in partially molten silicate systems at temperatures as low as 1175°C. This has also been reported by Otero Arean et al. (1997) with a quite different synthesis route consisting of controlled hydrolysis of mixed metal alkoxides, followed by calcination at 1046°C.

As a further complication, all our spinel analyses consistently contain SiO_2, from 1 wt% at 68 h to ca. 10 wt% at 10 min. Such SiO_2 contents in γ-Al_2O_3 have been reported by Devineau et al. (2006) from similar experiments in the absence of Zn. Tetravalent ions can be incorporated in spinel structures according to $2M^{3+}=M^{2+}+M^{4+}$. The solid solution of

titanomagnetites between magnetite and ulvospinel ($Fe^{2+}_2TiO_4$) is a well known example of such a substitution. Substitution by Si is less common but nevertheless known in natural and synthetic spinels. Huberty et al. (2012) report silician magnetite, and list various studies reporting up to 8 wt% SiO_2 in magnetite. Brindley and Nakahira (1959) and Eberhart (1963) early mentioned the occurrence of an Al-Si spinel phase formed from the decomposition of phyllosilicates. They proposed the formula of Si_8 [$Al_{32/3}$ $\square_{16/3}$] O_{32} and Si_8 [Al_8 $\square_8$] [O_{28} $\square_4$] for the spinel phase resulting from the decomposition of kaolinite (Brindley and Nakahira 1959) and muscovite (Eberhart 1963), respectively. More recently, various authors reported syntheses of γ-Al_2O_3 with 10-18 wt% SiO_2 (McHale et al. 1997; Schneider et al. 1994; Okada and Otsuka 1986; Sonuparlak et al. 1987), Chakraborty (1979, 1993, 2008) and Chakraborty and Das (2003) advocate the existence of a spinel end member with a $3Al_2O_3{\cdot}2SiO_2$ stoichiometry. The average analysis of γ-Al_2O_3 (Table 3) is perfectly stoichiometric, with Mg^{2+} compensating Si^{4+}. Stoichiometry is more difficult to evaluate for the Al-Zn phase because of vacancies, the uncertainty as to the valence state of Fe, and the analytical error. Special care was taken to record analyses only from the largest particles, and from those who seemed to go across the thickness of the FIB section, to avoid contamination by the glass. Most analyses, however, show small but significant contents of K, an element that is unlikely to enter the spinel structure. We consider that Si is truly incorporated in the γ-Al_2O_3 and Al-Zn spinel structures, but recognize that contamination by the surrounding glass can not be completely ruled out. Contrary to what was reported by Tkalcec et al. (2005), we do not observe a transitional Zn-Al-silicate as a precursor phase of gahnite.

Mullite is a minor product of muscovite destabilization that had also been identified in our previous Zn-free experiments at 40 min. The aluminous mullite composition (close to the $2Al_2O_3{\cdot}SiO_2$ stoichiometry) recorded here in the 10 min experiment, however, does not match the composition (close to the $3Al_2O_3{\cdot}2SiO_2$ stoichiometry) observed by Devineau et al.

443 (2006). This difference may be explained by the different durations, but these results are to be
444 taken with care considering the limited number of analyses in both cases and the fact that
445 EDS-TEM was performed on different instruments.
446
447 **Reaction pathway and kinetics of muscovite destabilization**
448 Equilibrium experiments in the K_2O-SiO_2-Al_2O_3 system (Yoder and Eugster 1955)
449 show that the expected destabilization products of anhydrous muscovite compositions are
450 leucite+K-feldspar+mullite at $T < 1140$°C, leucite+mullite+melt for $1140 < T < 1315$°C, and
451 leucite+corundum+melt at $T > 1315$°C. Other assemblages, however, have been described by
452 various authors (Roy 1949; Sundius and Byström 1953; Brindley and Maroney 1960;
453 Eberhart 1963; MacKenzie et al. 1987; Barlow and Manning 1999; Cultrone et al. 2001;
454 Rodriguez-Navarro et al. 2003). Many authors report the occurrence of metastable γ-Al_2O_3,
455 and the absence of leucite and K-feldspar (For explanations, see, e.g., Brindley and Maroney
456 1960; Eberhart 1963; Grapes 1986; Brindley and Lemaître 1987; Worden et al. 1987; Barlow
457 and Manning 1999; Sanchez-Navas 1999; Cultrone et al. 2001; Rodriguez-Navarro et al.
458 2003; Devineau et al. 2006).
459 In the Zn-free experiments (Devineau et al. 2006) on the same starting products, at the
460 same temperature and for similar durations (from 5 min to 68 h), muscovite was completely
461 destabilized after 5 min to γ-Al_2O_3, minor mullite, and melt; corundum appeared at 24 h. In
462 this study, γ-Al_2O_3, Al-Zn spinel and minor mullite are observed for 10 min durations, and
463 Zn-Al spinels close to gahnite are observed at 68 h.
464 For 10 min heating, the core of the muscovite pseudomorphs is still devoid of Zn, and γ-
465 Al_2O_3 with morphologies and compositions comparable to what was observed in the 5 min
466 Zn-free experiments of Devineau et al. (2006). In the rim of the muscovite pseudomorphs, Zn
467 enrichment produces an Al-Zn spinel phase with compositions intermediate between γ-Al_2O_3

and gahnite. The Zn profile in Figure 8 is typical of a diffusion profile. The Zn-enriched rims around muscovite pseudomorphs are rather constant along the perimeter of the grain, indicating that Zn diffused homogeneously despite the fact that it was initially heterogeneously distributed in the quartz-feldspar matrix. For 68 h duration, most muscovite pseudomorphs are chemically and texturally equilibrated. The spinel phase has a composition close to gahnite end-member, and crystals tend to be isometric in shape. Gahnite retains only minor SiO_2 content, contrary to γ-Al_2O_3 and the Al-Zn spinel. The fact that the melt compositions are enriched in SiO_2 at 68 h could be the consequence of the release of Si from the spinel phases or, alternatively, could be explained by diffusion of Si from the surrounding quartz-feldspar melt. The largest muscovite pseudomorphs, however, retain a fine-grained core with ZnO concentrations lower than in the rims, indicating that equilibrium is not completely reached after 68 h. The texture in these cores is comparable with the 10 min experiments, but crystals are larger and show a mottled contrast less pronounced in TEM images. The presence of Zn allows the formation of gahnite as a stable spinel structure, thus inhibiting the formation of corundum that was observed in the Zn-free system.

Devineau et al. (2006) described γ-Al_2O_3 crystallites as acicular and oriented along the {100} directions of the former muscovites. In this study, the use of oriented FIB foils allows a better investigation of morphologies. γ-Al_2O_3 crystallites appear elongated in the perpendicular cuts and irregularly shaped in longitudinal sections, indicating a flaky morphology with preferential orientation parallel to the former muscovite cleavages. This morphology and orientation are conserved in the Zn-enriched rims of the 10 min sample and in the core of the largest muscovites at 68 h. However, the orientation of the former muscovite a and b axes being unknown, the present experiments can not be used to discuss further the nature of the epitaxial orientation of the spinel phase. A tabular morphology, however, is not compatible with the observations on basal sections of Devineau et al. (2006; their Figs. 5 and

493 9). It can be reconciled, however, by considering that the "needles" observed in the basal
494 planes were sections of platelets lying at an angle with (001). Such out-of-plane platelets are
495 observed in the perpendicular and longitudinal FIB cuts (Figs. 3b, 5b, and left side of 6d).
496
497 **Relevance to heavy metals immobilization**
498 Industrial wastes have variable heavy metal contents, depending on their nature, from a
499 few hundred ppm (e.g., steelworks slags; Favoni et al. 2005) to thousands of ppm (e.g., 2850
500 ppm Zn in sewage sludge ash; Cheeseman et al. 2003; 0.52 wt% ZnO in fly ash from sewage
501 sludge incinerator; Park et al. 2003) or even several percents (e.g., 4.5 wt% Zn in dried
502 galvanic sludges; Magalhães et al. 2004a). In this study, we prepared a highly concentrated
503 (8.5 wt% ZnO) mixture of ZnO and granite powder in order to be able to follow the
504 distribution of Zn using high spatial resolution EDS analysis and thus understand the
505 mechanisms of incorporation of Zn in mineral phases.
506 This work demonstrates that Zn can be incorporated in crystalline spinel phases during
507 the firing of Zn-doped quartz-feldspar-muscovite powders at 1175°C, for durations as short as
508 10 min. Zn appears to diffuse and concentrate in the muscovite pseudomorphs, compared to
509 the quartz-feldspar matrix. The highest Zn concentrations in the muscovite pseudomorphs
510 reach 17 wt% ZnO. Diffusion fronts in the pseudomorphs are less that 1 micrometer large
511 after 10 min, and reach several hundred micrometers after 68 h. In mixtures containing a
512 larger proportion of fine-grained layer silicates (e.g., an illite-rich clay), it is to be expected
513 that Zn will be efficiently trapped in the destabilized layer silicates according to mechanisms
514 identical to those observed in this study. Such a stabilization mechanism has been
515 demonstrated by Shih et al. (2006), who reported on the formation of $NiAl_2O_4$ spinel obtained
516 from a mixture of kaolinite and NiO heated at 1250°C during 3 h.

517 For short durations of heat treatment, Zn is stored in intermediate Al-Zn spinels of the γ-
518 Al_2O_3-gahnite solid solution. γ-Al_2O_3 is a metastable phase relative to corundum. However, it
519 is relatively stable under ambient conditions (nano-crystalline γ-Al_2O_3 is an industrial product
520 used as a catalyst support and for other applications; see e.g., Zhou and Snyder 1991;
521 Urretavizcaya et al. 1998; Souza-Santos et al. 2000; Nicosia and Prins 2005; Liu et al. 2008).
522 Since in our experiments γ-Al_2O_3 nanoparticles are embedded in a glass phase within the
523 muscovite pseudomorphs, it is probable that Al-Zn spinels would be inert in the environment.
524 For longer durations at high temperatures, and because of the high concentration of ZnO in
525 the initial mixture, Zn stabilizes the spinel phase as gahnite and corundum is not observed to
526 form after 68 h at the expense of γ-Al_2O_3. For lower Zn contents in the spinel, however, it is
527 possible that intermediate Al-Zn spinels may not be stable relative to corundum and thus
528 could release their Zn content for long durations of heat treatment when transforming to
529 corundum.

530 As the present study deals with the incorporation of Zn in the destabilization products of
531 muscovite, the reaction products in the quartz-feldspar glass were not investigated in similar
532 detail. However it seems that Zn-containing spinel does not form in the molten quartz-
533 feldspar matrix, but willemite forms instead. This is probably due to the fact that quartz-
534 feldspar glass is too low in Al_2O_3 (18 wt% for 10 min and 15.5 wt% for 68h in Table 2)
535 compared with melts produced by the fusion of muscovite (34 wt% Al_2O_3, Table 2). It is
536 possible, however, that local chemical heterogeneities in the molten quartz-feldspar matrix
537 due to the presence of Al-rich clays favor the formation of Zn-rich spinel. Lee et al. (2005)
538 report gahnite from Zn-doped porcelain bodies, but examination of their starting compositions
539 suggest their melts also have a high Al_2O_3content. Hansson et al. (2005) revisited the Al_2O_3-
540 SiO_2-ZnO ternary phase diagram, first investigated by Bunting (1930, 1932). In the SiO_2-ZnO
541 binary, willemite has a wide field of stability, whereas gahnite is a stable phase on a major

542 part of the Al_2O_3-ZnO join. Sub-solidus topology of the ternary diagram, however, is
543 unknown for intermediate compositions. For SiO_2-rich compositions, the stable phase
544 willemite is to be expected rather than metastable Zn-rich spinel, but it is not possible to
545 predict its field of stability in relation with the Al_2O_3-SiO_2 composition. For Al-rich
546 compositions of glasses, as it is the case for muscovite pseudomorphs, it is probable that
547 willemite is no more a stable phase, and metastable Zn-rich spinel, then gahnite, forms
548 instead. Furthermore, the former muscovite structure provides, through epitaxial nucleation,
549 an energetically efficient way to avoid the expense of most of the activation nucleation thus
550 promoting the formation of a Zn-rich metastable spinel phase. The local presence of H_2O
551 from muscovite dehydroxylation accelerates the diffusion of Zn, compared to dry quartz-
552 feldspar glass. Consequently, the Zn-spinel preferentially form in the Ms-pseudomorph.
553 Because of the variety of the spinel group crystal chemistry, other heavy metals (Co, Cr,
554 Ni, V...) may also be concentrated and stabilized in the decomposition phases of layer
555 silicates. Usually stable under ambient conditions, spinel-group minerals should be considered
556 prime candidates for the immobilization of heavy metals.
557

558 **ACKNOWLEDGEMENTS**

559 The authors are indebted to the reviewers for their constructive comments and
560 suggestions that contributed to improve this article. Assistance by J. Ravaux on the electron
561 microprobe and by L. Mouton on the scanning electron microscopy are gratefully
562 acknowledged. The authors thank D. Troadec for the preparation of FIB cuts at IEMN, Lille.
563 TEM work was performed at the CNRS-INSU French National Facility for electron
564 microscopy at UMET, Lille. K.D. acknowledges University of Lorraine and Region Lorraine
565 for the financial support.
566

REFERENCES CITED

Barlow, S.G. and Manning, D.A.C. (1999) Influence of time and temperature on reactions and transformations of muscovite mica. British Ceramic Transactions, 98, 122.126.

Basegio, T., Berutti, F., Bernardes, A., and Bergmann, C. P. (2002) Environmental and technical aspects of the utilisation of tannery sludge as a raw material for clay products. Journal of the European Ceramic Society, 22, 2251-2259.

Brindley, G.W. and Lemaître, J. (1987) Thermal, oxidation and reduction reactions of clay minerals. In A.C.D. Newman, Ed., Chemistry of clays and clay minerals, p. 319-370. Mineralogical Society Great Britain Monograph, 6, London.

Brindley, G.W. and Maroney, D. (1960) High-temperature reactions of clay mineral mixtures and their ceramic properties: II, reactions of kaolinite-mica-quartz mixtures compared with the K_2O-Al_2O_3-SiO_2 equilibrium diagram. Journal of the American Ceramic Society, 43, 511-516.

Brindley, G.W. and Nakahira, M. (1959) The kaolinite-mullite reaction series: I, Survey of outstanding problems. II, Metakaolin. III, The high-temperature phases. Journal of the American Ceramic Society, 42, 311-324.

Bruhns, P. and Fischer, R.X. (2001) Phase reactions in the brick firing process of V-doped clay. European Journal of Mineralogy, 13, 611-619.

Bunting, E.N. (1930) Phase Equilibria in the System SiO_2-ZnO. Bureau of Standards Journal of Research, 4, 131-36.

Bunting, E.N. (1932) Phase Equilibria in the System SiO_2-ZnO-Al_2O_3. Bureau of Standards Journal of Research, 8, 279-87.

Chakraborty, A.K. (1979) Formation of Silicon-Aluminum Spinel. Journal of the American Ceramic Society, 62, 120-124.

591 Chakraborty, A.K. (1993) Intermediate Si-Al spinel phase formation in phase transformation
592 of diphasic mullite gel. Journal of Materials Science, 28, 3839-3844.
593 Chakraborty, A.K. (2008) Si-incorporated alumina phases formed out of diphasic mullite gels.
594 Journal of Materials Science, 43, 5313-5324.
595 Chakraborty, A.K. and Das, S. (2003) Al-Si spinel phase formation in diphasic mullite gels.
596 Ceramics International, 29, 27-33.
597 Cultrone, G., Rodriguez-Navarro, C., Sebastian, E., Cazalla, O., and de la Torre, M.J. (2001)
598 Carbonate and silicate phase reactions during ceramic firing. European Journal of
599 Mineralogy, 13, 621-634.
600 Cusido, J.A., Cremades, L.V., and Gonzalez, M. (2003) Gaseous emissions from ceramics
601 manufactured with urban sewage sludge during firing processes. Waste Management,
602 23, 273-280.
603 Devineau, K., Pichavant, M., and Villiéras, F. (2005) Melting kinetics of granitic powder
604 aggregates at 1175°C, 1 atm. European Journal of Mineralogy, 17, 387-398.
605 Devineau, K., Devouard, B., Villiéras F., Faure, F., Devidal, J.L., and Kohler, A. (2006)
606 Evolution of product phase assemblages during thermal decomposition of muscovite
607 under strong disequilibrium conditions. American Mineralogist, 91, 413-424.
608 Devineau, K., Villiéras, F., and Barrès O. (2007) Development and evolution of water vapor
609 vesicles during fast thermal breakdown of muscovite. Physics and Chemistry of
610 Minerals, 34, 559-572.
611 Donald, I.W. (2010) Waste Immobilization in Glass and Ceramic Based Hosts: Radioactive,
612 Toxic, and Hazardous Wastes. Wiley, New York.
613 Eberhart, J. (1963) Transformation de la muscovite par chauffage entre 700 et 1200°C.
614 Bulletin de la Société Française de Minéralogie et de Cristallographie, 86, 213-251.

615 Ferreira, C., Ribeiro, A., and Ottosen, L. (2003) Possible applications for municipal solid
616 waste fly ash. Journal of Hazardous Materials, B96, 201-216.
617 Grapes, R.H. (1986) Melting and Thermal Reconstitution of Pelitic Xenoliths, Wehr Volcano,
618 East Eifel, West Germany. Journal of Petrology, 27, 343-396.
619 Gutiérrez, G., Taga, A., and Johansson, B. (2001) Theoretical structure determination of γ-
620 Al_2O_3. Physical Review B, 65, 0121011-0121014.
621 Haiying, Z., Youcai, Z., and Jingyu, Q. (2011) Utilization of municipal solid waste
622 incineration (MSWI) fly ash in ceramic brick: Product characterization and
623 environmental toxicity. Waste Management, 31, 331-341.
624 Hamer, K. and Karius, V. (2002) Brick production with dredged harbour sediments. An
625 industrial-scale experiment. Waste Management, 22, 521-530.
626 Hansson, R., Hayes P.C., Jak, E. (2004) Experimental Study of Phase Equilibria in the Al-Fe-
627 Zn-O System in Air. Mettallurgical and Materials Transactions B, 35B, 633-642.
628 Hansson, R., Zhao, B., Hayes P.C., Jak, E. (2005) A Reinvestigation of Phase Equilibria in
629 the System Al_2O_3-SiO_2-ZnO. Mettallurgical and Materials Transactions B, 36B, 187-
630 193.
631 Hojamberdiev, M., Eminov, A., and Xu, Y. (2011) Utilization of muscovite granite waste in
632 the manufacture of ceramic tiles. Ceramics International, 37, 871-876.
633 Hu, C.Y., Shih, K., and Leckie, J.O. (2010) Formation of copper aluminate spinel and cuprous
634 aluminate delafossite to thermally stabilize simulated copper-laden sludge. Journal of
635 Hazardous Materials, 181, 399-404.
636 Huberty, J.M., Konishi, H., Heck, P.R., Fournelle, J.H., Valley, J.W., and Xu, H. (2012)
637 Silician magnetite from the Dales Gorge Member of the Brockman Iron Formation,
638 Hamersley Group, Western Australia. American Mineralogist, 97, 26-37.

639 Jordan, M.M., Almendro-Candel, M.B., Romero, M., and Rincon, J.Ma. (2005) Application
640 of sewage sludge in the manufacturing of ceramic tile bodies. Applied Clay Science, 30,
641 219-224.
642 Lee, S.M., Kim, S.K., Yoo, J.W., Kim, H.T. (2005) Crystallization behavior and mechanical
643 properties of porcelain bodies containing zinc oxide additions. Journal of the European
644 Ceramic Society, 25, 1829-1834.
645 Leroux, H., Stroud, R.M., Dai, Z.R., Graham, G.A., Troadec, D., Bradley, J.P., Teslich, N.,
646 Borg, J., Kearsley, A.T., and Hörz, F. (2008) Transmission electron microscopy of
647 cometary residues from micron-sized craters in the Stardust Al foils. Meteoritics &
648 Planetary Science, 43, 143-160.
649 Lide, D.R. (2008) CRC Handbook of chemistry and physics: a ready-reference book of
650 chemical and physical data (88th edition). CRC Press , p.4-134.
651 Liu, Q., Wang, A., Wang, X., Gao, P., Wang, X., and Zhang, T. (2008) Synthesis,
652 characterization and catalytic applications of mesoporous γ-alumina from boehmite sol.
653 Microporous and Mesoporous Materials, 111, 323-333.
654 Mackenzie, K.J.D., Brown, I.W.N., Cardile, C.M., and Meinhold, R.H. (1987) The thermal
655 reactions of muscovite studied by high resolution solid-state 29-Si and 27-Al NMR.
656 Journal of Materials Science, 22, 2645.2654.
657 Magalhães, J.M., Silva, J.E., Castro, F.P., and Labrincha, J.A. (2004a) Effect of experimental
658 variables on the inertization of galvanic sludges in clay-based ceramics. Journal of
659 Hazardous Materials, 106B, 139-147.
660 Magalhães, J.M., Silva, J.E., Castro, F.P., and Labrincha, J.A. (2004b) Role of the mixing
661 conditions and composition of galvanic sludges on the inertization process in clay-based
662 ceramics. Journal of Hazardous Materials, 106B, 169-176.

663 Magalhães, J.M., Silva, J.E., Castro, F.P., and Labrincha, J.A. (2005) Kinetic study of the
664 immobilization of galvanic sludge in clay-based matrix. Journal of Hazardous
665 Materials, B121, 69-78.
666 McHale, J.M., Yürekli, K., Dabbs, D.M., Navrotsky, A., Sundaresan, S., and Aksay, A.I.
667 (1997) Metastability of spinel-type solid solutions in the SiO_2-Al_2O_3 system. Chemistry
668 of Materials, 9, 3096-3100.
669 Menezes, R.R., Ferreira, H.S., Neves, G.A., Lira, H.L., and Ferreira, H.C. (2005) Use of
670 granite sawing wastes in the production of ceramic bricks and tiles. Journal of the
671 European Ceramic Society, 25, 1149-1158.
672 Merino, I., Arévalo, L.F., and Romero, F. (2007) Preparation and characterization of ceramic
673 products by thermal treatment of sewage sludge ashes mixed with different additives.
674 Waste Management, 27, 1829-1844.
675 Monteiro, S.N., Peçanha, L.A., and Vieira, C.M.F. (2004) Reformulation of roofing tiles body
676 with addition of granite waste from sawing operations. Journal of the European Ceramic
677 Society, 24, 2349-2356.
678 Montero, M.A., Jordán, M.M., Hernández-Crespo, M.S., and Sanfeliu, T. (2009) The use of
679 sewage sludge and marble residues in the manufacture of ceramic tile bodies. Applied
680 Clay Science, 46, 404-408.
681 Nicosia, D. and Prins, R. (2005) ^{31}P MAS NMR and Raman study of a Co(Zn)MoP/γ-Al_2O_3
682 HDS catalyst precursor containing triethylene glycol. Journal of Catalysis, 234, 414-
683 420.
684 Okada, K. and Otsuka, N. (1986) Characterization of the Spinel Phase from SiO_2-Al_2O_3
685 Xerogels and the Formation Process of Mullite. Journal of the American Ceramic
686 Society, 69 [9], 652-56.

687 Otero Arean, C., Sintes Sintes, B., Turnes Palomino, G., Mas Carbonell, C., Escalona Platero,
688 E., and Parra Soto, J.B. (1997) Preparation and characterization of spinel-type high
689 surface area Al_2O_3-$ZnAl_2O_4$ mixed metal oxides by an alkoxide route. Microporous
690 Materials, 8, 187-192.
691 Overwijk, M.H.F., van den Heuvel, F.C., and Bulle-Lieuwma, C.W.T. (1993) Novel scheme
692 for the preparation of transmission electron microscopy specimens with a focused ion
693 beam. Journal of Vaccum Science and Technology B, 11, 2021-2024.
694 Pichavant, M. and Manning, D.A.C. (1984) Petrogenesis of tourmaline granites and topaz
695 granites: the contribution of experimental data. Physics of the Earth and Planetary
696 Interiors, 35, 31-50.
697 Pouchou, J.L., and Pichoir, F. (1991) Quantitative analysis of homogeneous or stratified
698 microvolumes applying the model "PAP". In K.F.J. Heinrich and D.E. Newbury, Eds.,
699 Electron probe quantification, p. 31-75. Plenum Press, New York.
700 Reinosa, J.J., Silva, A.C., Rubio-Marcos, F., Mello-Castanho, S.R.H., Moya, J.S., and
701 Fernandez, J.F. (2010) High chemical stability of stoneware tiles containing waste
702 metals. Journal of the European Ceramic Society, 30, 2997-3004.
703 Rodriguez-Navarro, C., Cultrone, G., Sanchez-Navas, A., and Sebastian, E. (2003) TEM
704 study of mullite growth after muscovite breakdown. American Mineralogist, 88, 713-
705 724.
706 Roy, R. (1949) Decomposition and resynthesis of the micas. Journal of the American Ceramic
707 Society, 32, 202-209.
708 Sanchez-Navas, A. (1999) Sequential kinetics of a muscovite-out reaction: A natural example.
709 American Mineralogist, 84, 1270-1286.

710 Schneider, H., Voll, D., Saruhan, B., Schmücker, M., Schaller, T., and Sebald, A. (1994)
711 Constitution of the γ-Alumina Phase in Chemically Produced Mullite Precursors.
712 Journal of the European Ceramic Society, 13, 441-448.
713 Shih, K., White, T., and Leckie, J.O. (2006) Spinel Formation for Stabilizing Simulated
714 Nickel-Laden Sludge with Aluminum-Rich Ceramic Precursors. Environmental Science
715 & Technology, 40, 5077-5083.
716 Shih, K. and Leckie, J.O. (2007) Nickel aluminate spinel formation during sintering of
717 simulated Ni-laden sludge and kaolinite. Journal of the European Ceramic Society, 27,
718 91-99.
719 Silva, A.C., and Mello-Castanho, S.R.H. (2004) Silicate glasses obtained from fine silica
720 powder modified with galvanic waste addition. Journal of Non-Crystalline Solids, 348,
721 211-217.
722 Silva, A.C., and Mello-Castanho, S.R.H. (2007) Vitrified galvanic waste chemical stability.
723 Journal of the European Ceramic Society, 27, 565-570.
724 Silva, A.C., Mello-Castanho, S., Guitian, F., Montero, I., Esteban-Cubillo, A., Sobrados, I.,
725 Sanz, J., and Moya, J.S. (2008) Incorporation of Galvanic Waste (Cr, Ni, Cu, Zn, Pb) in
726 a Soda-Lime-Borosilicate Glass. Journal of the American Ceramic Society, 91 [4],
727 1300-1305.
728 Silva, A.C., Reinosa, J.J., Moya, J.S., Fernandez, J.F., and Mello-Castanho, S.R.H. (2010)
729 Green stoneware containing waste metals. Materials Science Forum, 660-661, 730-736.
730 Sonuparlak, B., Sarikaya, M., and Aksay, I.A. (1987) Spinel Phase Formation During the
731 980°C Exothermic Reaction in the Kaolinite-to-Mullite Reaction Series. Journal of the
732 American Ceramic Society, 70 [11], 837-42.
733 Souza-Santos, P., Souza-Santos, H., and Toledo, S.P. (2000) Standard transition aluminas.
734 Electron microscopy studies. Materials Research, 3, 104-114.

735 Sundius, N. and Byström, A.M. (1953) Decomposition products of muscovite at temperatures
736 between 1000 and 1260°C. Transactions of the British Ceramic Society, 52, 632-642.
737 Tellefsen, M., Carreiro, L., Kershaw, R., Dwight, K., and Wold, A. (1984) Homogeneity and
738 Magnetic Susceptibility in Some Substituted Cadmium Spinels. The Journal of Physical
739 Chemistry, 88, 754-756.
740 Tkalcec, E., Kurajica, S., and Ivankovic, H. (2005) Crystallization behavior and
741 microstructure of powdered and bulk ZnO-Al_2O_3-SiO_2 glass-ceramics. Journal of Non-
742 Crystalline Solids, 351, 149−157.
743 Torres, P., Manjate, R.S., Quaresma, S., Fernandes, H.R., and Ferreira, J.M.F. (2007)
744 Development of ceramic floor tile compositions based on quartzite and granite sludges.
745 Journal of the European Ceramic Society, 27, 4649-4655.
746 Urretavizcaya, G., Cavalieri, A.L., Porto Lopez, J.M., Sobrados, I., and Sanz, J. (1998)
747 Thermal Evolution of Alumina Prepared by the Sol-Gel Technique. Journal of Materials
748 Synthesis and Processing, 6, 1-7.
749 Van Cappellen, E. (1990) The parameterless correction method in X-ray microanalysis.
750 Microscopy Microanalysis Microstructure, 1, 1-22.
751 Vieira, C.M.F. and Monteiro, S.N. (2006) Incorporation of granite waste into vitrified ceramic
752 tiles. Materials Science Forum, 530-531, 467-472.
753 Wirth, R. (2004) Focused Ion Beam (FIB): A novel technology for advanced application of
754 micro- and nanoanalysis in geosciences and applied mineralogy. European Journal of
755 Mineralogy, 16, 863-876.
756 Worden, R.H., Champness, P.E., and Droop, G.T.R. (1987) Transmission electron
757 microscopy of the pyrometamorphic breakdown of phengite and chlorite. Mineralogical
758 Magazine, 51, 107-121.

759 Yoder, H.S. and Eugster, H.P. (1955) Synthetic and natural muscovites. Geochimica
760 Cosmochimica Acta, 8, 225-280.
761 Zhou, R.S. and Snyder, R.L. (1991) Structures and transformation mechanisms of the eta,
762 gamma and theta transitions aluminas. Acta Crystallographica, B 47, 617-630.
763
764

765 **TABLE CAPTIONS**

766 **TABLE 1.** Bulk compositions (ICP-AES) of untreated and heat-treated samples (oxide wt%).

767 **TABLE 2.** Electron-microprobe analyses (oxide wt%) of unheated muscovite (Ms),
768 muscovite pseudomorphs, and glasses around muscovite pseudomorphs.

769 **TABLE 3.** TEM-EDS analyses (oxide wt%) of product phases from muscovite pseudomorphs
770 in the heat-treated samples. Analyses are normalized to 100%.

771 **FIGURE CAPTIONS**

772 **FIGURE 1.** BSE-SEM image showing the heterogeneous repartition of ZnO (white area)
773 before heating and local aggregation of ZnO at the surface of muscovite (Ms).

774

775 **FIGURE 2.** BSE-SEM images showing lateral sections of muscovite heated at 1175°C for (**a**)
776 10 min, (**c**) 40 min, and (**e**) 68 h. **b**, **d**, and **f** images show enlargements of the areas framed in
777 **a**, **c**, and **e**, respectively. Location of the longitudinal and perpendicular FIB cuts are visible in
778 **(a)** and **(e)**. Muscovite is completely replaced by sub-micrometric product phases disposed in
779 parallel alignments that outline the cleavage directions of the former muscovites. Some
780 elongated crystallites are not parallel to the former cleavages and display an orientation
781 roughly at 120°. For the short duration runs (**b** and **d**), the muscovite pseudomorphs (Ps) are
782 systematically outlined by coarser oxides enriched in Zn. At the core of the Ps, crystallites
783 appear to have uniform sizes, ca. 50 nm large and up to ca. 600 nm in the longer direction.
784 Crystallites in the rims have similar morphologies and orientation, but display a brighter BSE
785 contrast and are somewhat thicker: up to 70 x 500 nm at 10 min and 200 x 1000 nm at 40 min.
786 **(e)** In the 68 h run, a large Ps (300 μm) displays core-rim differences. **(f)** The rim texture
787 displays well individualized Zn-Al oxides within a homogeneous Si-Al-rich phase.
788 Crystallites are coarser (ca. 0.3 x 1.3 μm) and less elongated than in the short duration runs.

789 The core retains a texture similar to what was observed in the rims for the short duration runs,
790 with mostly oriented elongated oxides ca. 80 x 900 nm.
791
792 **FIGURE 3.** TEM images showing reaction products in the longitudinal FIB cut of muscovite
793 heated for 10 min at 1175°C. (**a**) Assemblage of three bright-field STEM images covering the
794 whole longitudinal FIB cut. This view displays a homogeneous texture. (**b**) Enlargement of
795 the area framed in **a**, showing irregularly shaped crystals from a few tens of nm up to ca. 0.6 x
796 1.2 μm, and elongated crystals, ca. 20 x 300 nm, roughly oriented at 120° along three
797 directions. **(c)** Bright-field TEM image of a large irregularly shaped crystal with a mottled
798 contrast. **(d)** SAED patterns of the crystal in **c**, indexed as a spinel structure in the $[\bar{1}\,\bar{1}\,4]$
799 zone-axis.
800
801 **FIGURE 4.** SAED pattern of oxides in 10 min muscovite pseudomorphs. (**a**) Pattern recorded
802 using a large selection aperture in order to get a ring pattern from a large number of crystals in
803 various orientations from an area covering about the full width of the TEM foil (selection area
804 diameter = 6 μm). (**b**) Integrated radial intensity extracted from the above SAED pattern in
805 order to obtain a diffraction profile similar to what could be obtained from powder diffraction
806 data. **(c)** Comparison of peak positions from the radial SAED profile with the expected d_{hkl}
807 values of a spinel (gahnite from ICDD PDF file #5-669).
808
809 **FIGURE 5.** TEM images showing reaction products in the transversal FIB cut of muscovite
810 heated for 10 min at 1175°C. (**a**) Assemblage of two bright-field STEM images covering the
811 whole FIB cut, showing elongated, parallel crystals 10-80 nm wide and up to 1000 nm in
812 length, and rare crystals with a different morphology, euhedral and frequently skeletal
813 (arrowed). Matrix of quartz-feldspar glass and some relict quartz can be observed on the rim

814 of the pseudomorph. At the limit between the matrix and the pseudomorph, crystals of
815 willemite (as determined by EDS) display euhedral, hexagonal shapes. EDS mapping from
816 the framed area is shown in Fig. 8. (**b and c**) Bright-field TEM images of roughly parallel
817 elongated crystals with some outliers oriented at an angle from the general direction of
818 elongation, and a minor amount of shorter crystals. All those crystals have similar aspects and
819 frequently display mottled contrasts. (**d**) TEM image of a few of the skeletal crystal with
820 sharp diffraction contrast arrowed in **a**. (**e**) SAED pattern recorded from a large elongated
821 crystal in two different orientations, indexed as a spinel structure in the $[\bar{1}12]$ zone-axis. (**f**)
822 SAED pattern of the skeletal crystal in **d**, indexed as mullite in the [001] zone-axis.
823
824 **FIGURE 6.** TEM images showing reaction products in the longitudinal FIB cuts of
825 muscovite heated for 68 h at 1175°C. (**a**) Assemblage of two bright-field STEM images
826 covering the whole longitudinal FIB cut from the homogenous region (representative of most
827 pseudomorphs) and showing only large crystals, ca. 0.7 x 1 μm with peculiar subhedral
828 morphologies. (**b**) Bright-field TEM image of a few large crystals. (**c**) SAED pattern indexed
829 as gahnite in the [111] zone-axis. (**d**) Assemblage of two bright-field STEM images covering
830 the second longitudinal FIB cut, showing varied textures. The external region, cut within the
831 homogeneous, coarse grained rim, shows large gahnite crystals identical to what was
832 observed in the first longitudinal section. The core region contains both large irregular
833 crystals ca. 0.3 x 0.5 μm and some elongated crystals ca. 42 x 700 nm in a texture similar to
834 what was observed in the longitudinal section of the 10 min sample (Figs. 3a and 3b).
835
836 **FIGURE 7.** TEM images showing reaction products in the transversal FIB cut of muscovite
837 heated for 68 h at 1175°C. (**a**) Assemblage of three bright STEM images covering the
838 transversal FIB cut, showing a gradient of texture from the external rim (with large crystals

839 similar to those in the homogeneous longitudinal cut of Fig. 6a) to the core of the
840 pseudomorph (with euhedral, elongated crystals ca. 40 x 600 nm, similar to those observed in
841 the transversal cut of the 10 min sample, Fig. 5). (**b**) TEM bright-field image of the area
842 framed on the left of **a**. (**c**) SAED pattern of elongated crystals as in **b**, indexed as gahnite in
843 the [110] zone-axis. (**d**) TEM bright-field image of the area framed on the right of **a**. SAED
844 from these crystals (not shown) also indicate a spinel structure.
845
846 **FIGURE 8.** EDS mapping of the area framed in Fig. 5, through the Zn-enriched rim of a
847 muscovite pseudomorph heated at 1175°C for 10 min. (**a**) Spectral map of Zn recorded in
848 STEM mode, with a counting time of 400 msec by pixel and a spatial resolution of 14 nm. A
849 color-coded (R-G-B = Zn-Al-Si) version of this map is available as Supplemental Figure A3.
850 (**b**). Quantitative EDS profile reconstructed from the spectral map in **a**, along the direction
851 indicated by the arrow. Each data point averages a vertical stripe of 300 x 7 pixels (4200 x
852 110 nm). Zn concentrations decrease from 16 wt% at the edge of the pseudomorph to 0.5 wt%
853 ZnO at a distance of 3.5 μm from the edge.
854
855 **FIGURE 9.** TEM-EDS analyses of product phases in muscovite pseudomorphs for 10 min
856 and 68 h heating durations, projected in the SiO_2-Al_2O_3-ZnO diagram (molar proportions).
857 Analyses were acquired in STEM mode, either as point analyses, scanning over a small
858 region, or extracted from recorded spectral maps. The position of end-members minerals is
859 also indicated (small black circles).

Supplemental Figure A1. BSE-SEM image showing a basal section of muscovite heated for 40 min at 1175°C. The texture in the core displays complex heterogeneous mixtures of oxides with small crystallites ca. 50 to 300 nm, elongated crystals (50-100 nm x 2-3 μm) and hollow, euhedral crystals (0.5 x 1 μm).

Supplemental Figure A2. BSE-SEM images showing craters of the FIB cuts extracted out of lateral sections of heated muscovite, parallel (labeled Long.) and perpendicular (labeled Trans.) to the direction of the former muscovite (Ms) cleavages in two crystals selected from the optical and SEM observations (see FIB cut craters on Figs 2a and 2e). **(a)** For Ms heated during 10 min, the longitudinal FIB cut was carried out in the core region of the pseudomorph (Ps) but close to the rim (ca. 5 micrometers from the edge of the Ps) and **(b)** the transversal foil was cut across the rim and several micrometers into the core. **(c)** For the 68 h duration, a first longitudinal FIB cut was realized in an homogenous region representative of most Ps. A second longitudinal cut and a transversal cut were made in a large Ps to observe the transition between the coarse-grained rim and the finer-grained core.

Supplemental Figure A3. Color-coded (R-G-B = Zn-Al-Si) version of STEM-EDS elemental map in Fig. 8a (transversal cut through the thin Zn-rich rim).

Supplemental Figure A4. ZnO vs. Al_2O_3 contents (in wt%) of Al-Zn oxides in muscovite pseudomorphs after10 min at 1175°C (TEM-EDS analyses).

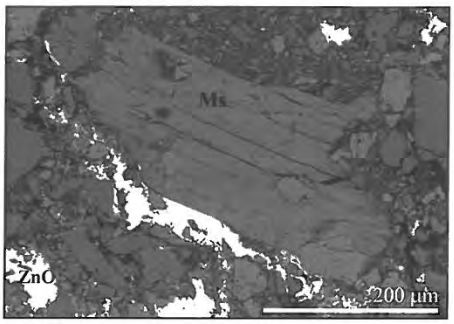

FIGURE 1.

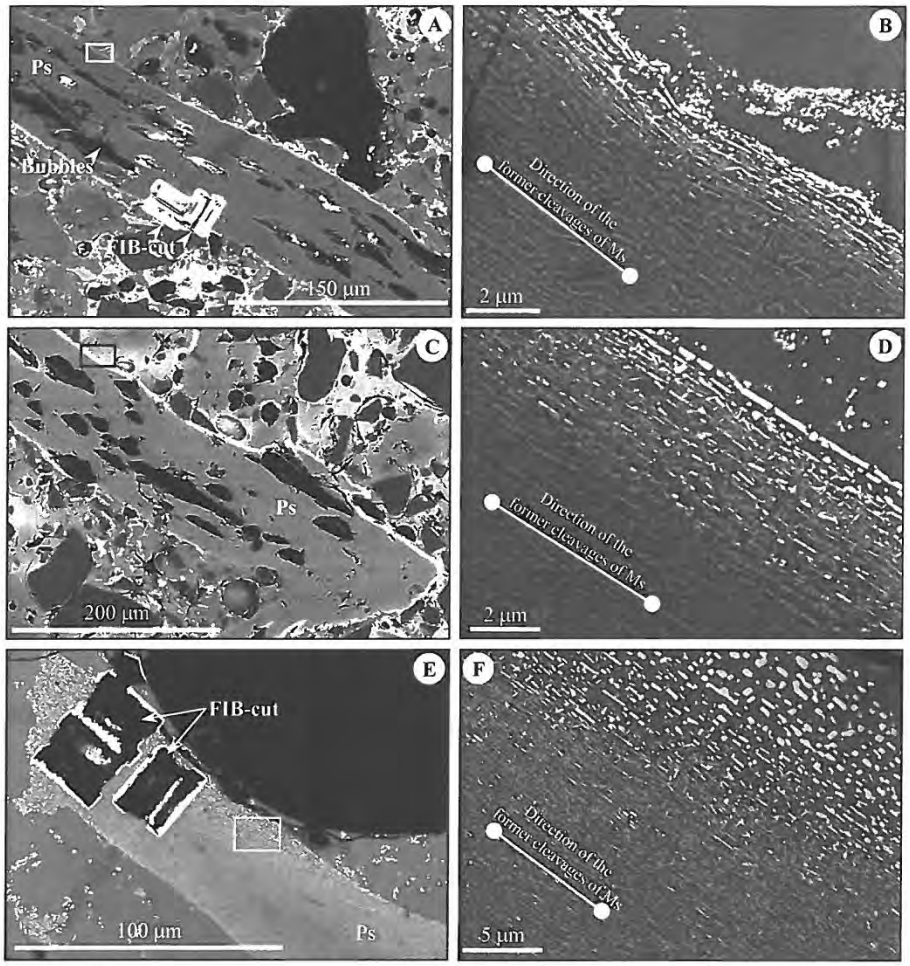
A
Ps
Bubbles
FIB-cut
150 µm
B
Direction of the former cleavages of Ms
2 µm
C
Ps
200 µm
D
Direction of the former cleavages of Ms
2 µm
E
FIB-cut
100 µm
Ps
F
Direction of the former cleavages of Ms
5 µm

FIGURE 2.

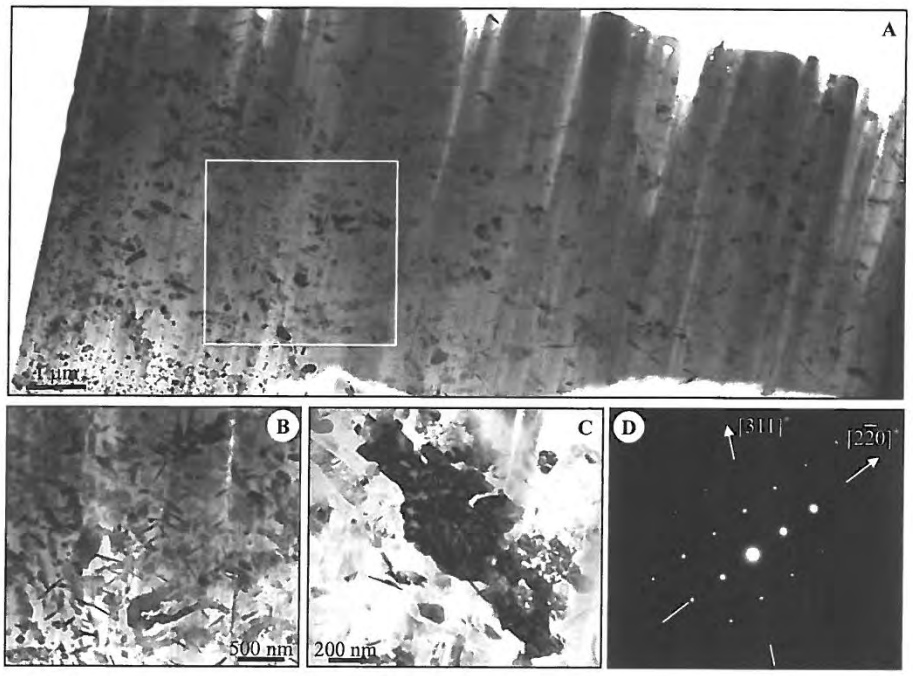

FIGURE 3.

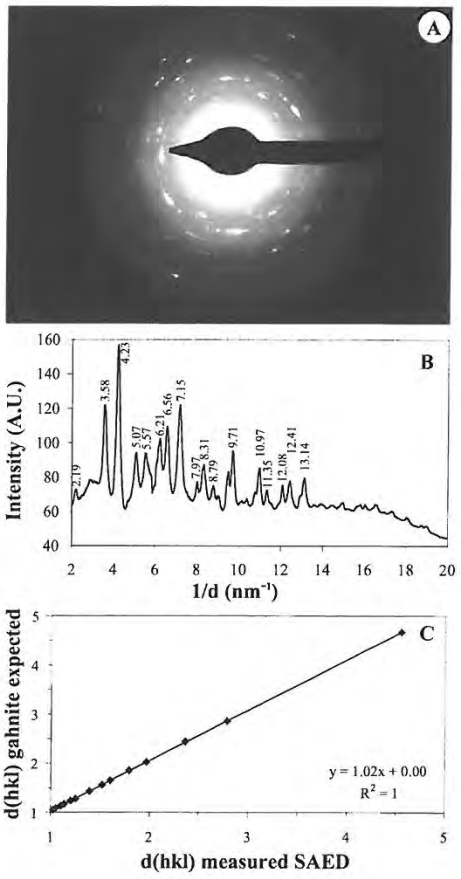
A
B
Intensity (A.U.)
1/d (nm⁻¹)
2.19
3.58
4.23
5.07
5.57
6.21
6.56
7.15
7.97
8.31
8.79
9.71
10.97
11.5
12.08
12.41
13.14
C
d(hkl) gahnite expected
d(hkl) measured SAED
y = 1.02x + 0.00
R² = 1

FIGURE 4.

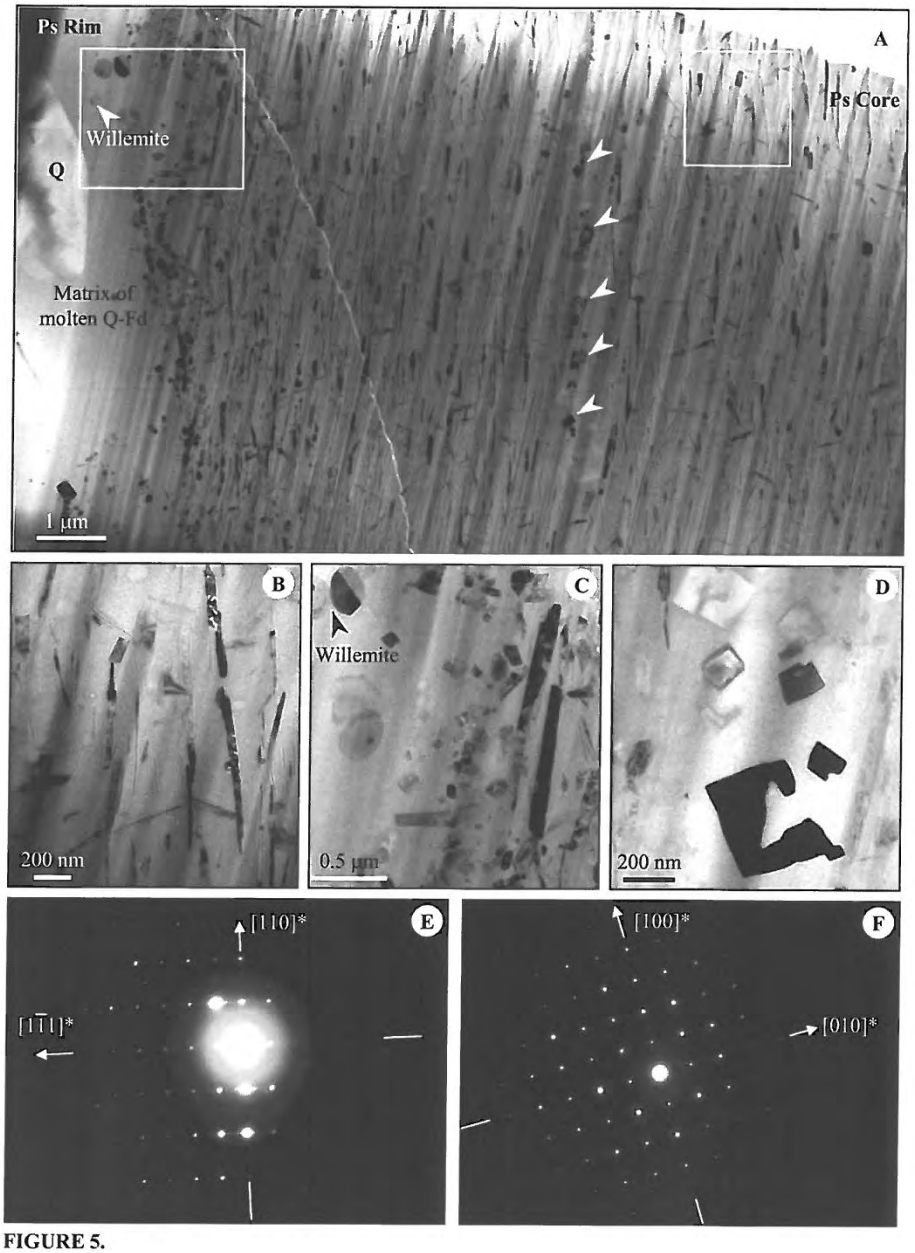
Ps Rim
A
Willemite
Q
Ps Core
Matrix of
molten Q-Fd
1 μm
B
200 nm
C
Willemite
0.5 μm
D
200 nm
[110]*
E
[1$\bar{1}$1]*
[100]*
F
[010]*

FIGURE 5.

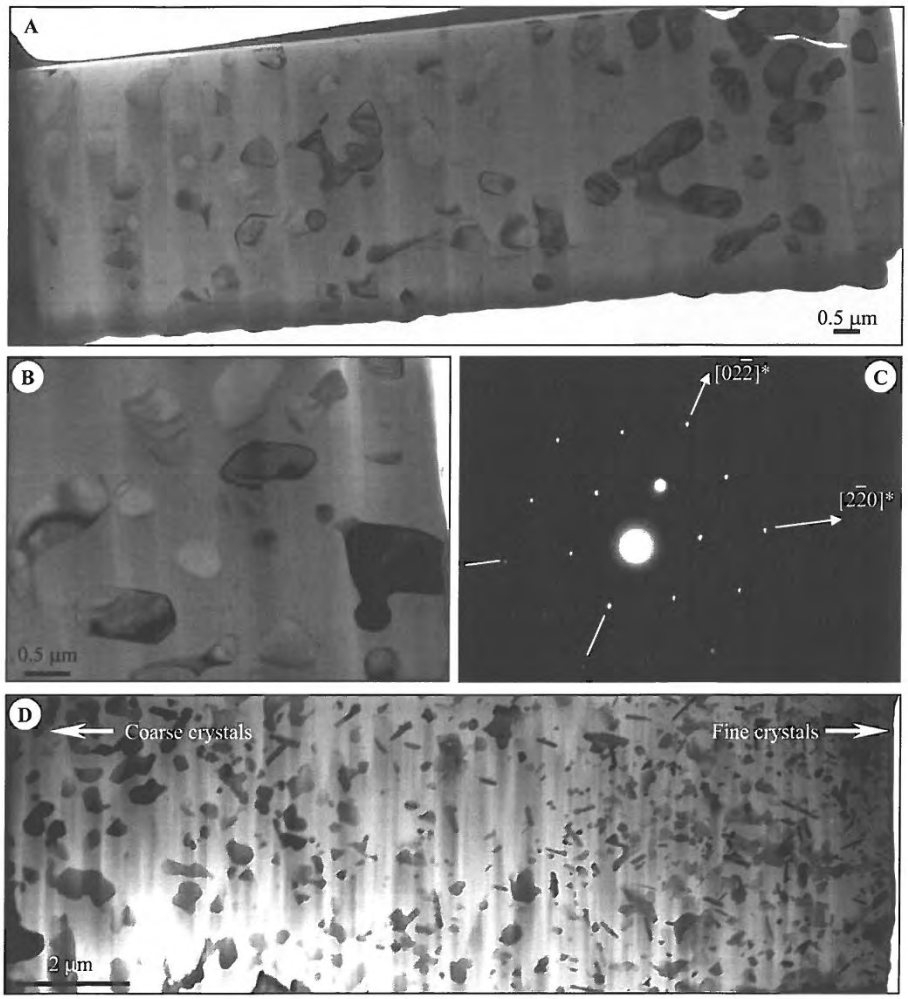

FIGURE 6.

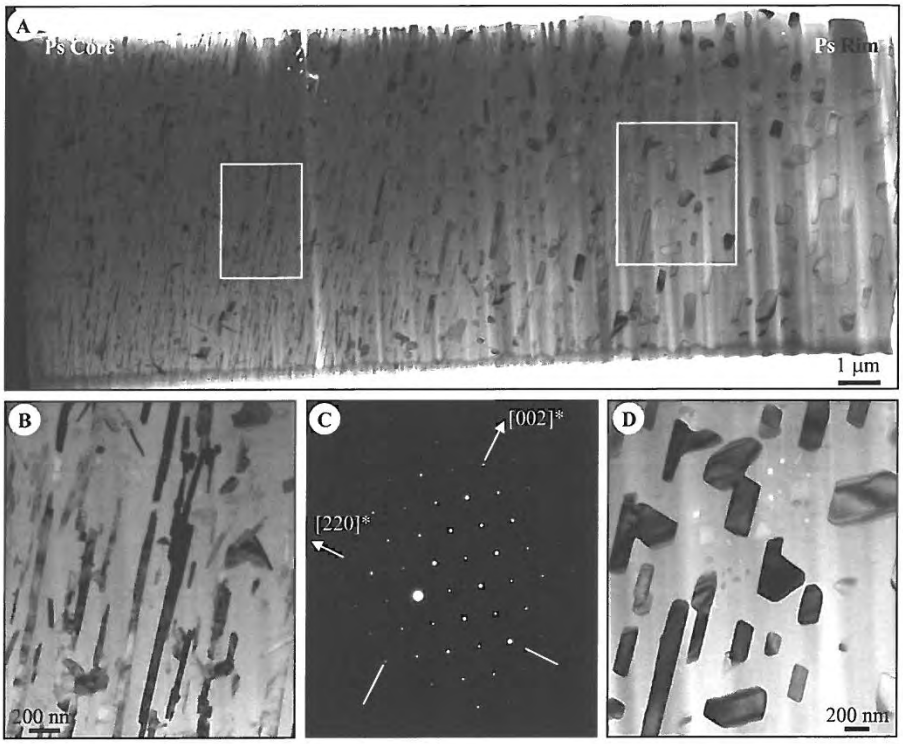

FIGURE 7.

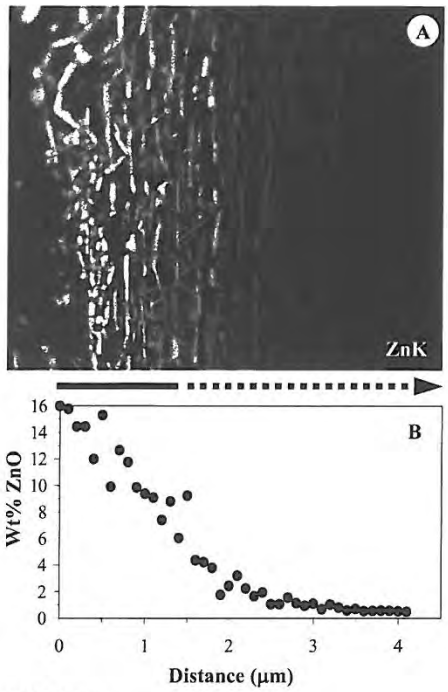

FIGURE 8.

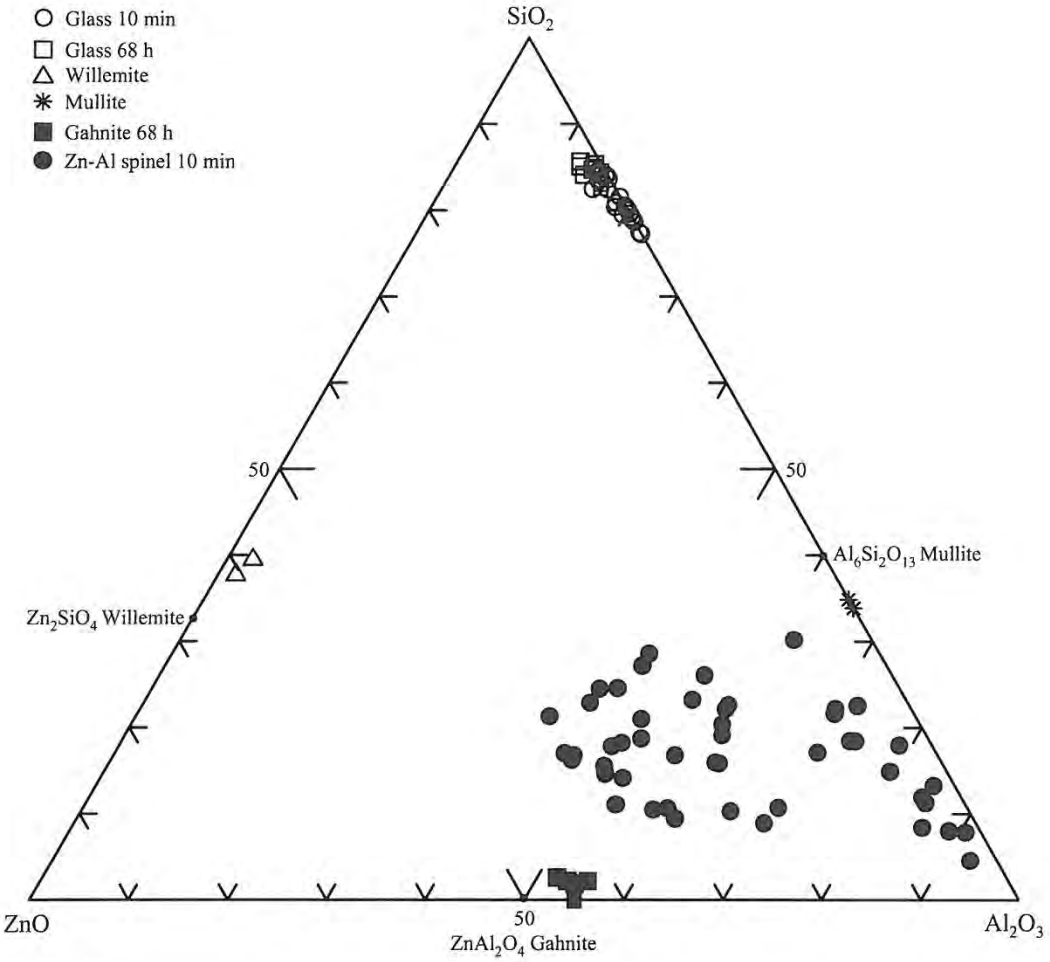
Glass 10 min
Glass 68 h
Willemite
Mullite
Gahnite 68 h
Zn-Al spinel 10 min
SiO2
50
50
Al6Si2O13 Mullite
Zn2SiO4 Willemite
ZnO
50
ZnAl2O4 Gahnite
Al2O3

FIGURE 9.

TABLE 1. Bulk compositions (ICP-AES) of untreated and heat-treated samples (oxide wt%)

	Before Heating	1175°C 10 min	1175°C 40 min	1175°C 68h
SiO_2	70.87	70.62	72.49	71.39
Al_2O_3	12.01	12.05	12.38	12.11
Fe_2O_3-T	0.33	0.32	0.32	0.32
MnO	0.02	0.01	0.01	0.01
MgO	0.14	0.14	0.14	0.14
CaO	0.28	0.25	0.26	0.25
Na_2O	2.87	2.88	2.96	2.90
K_2O	3.75	4.00	4.12	4.04
TiO_2	0.06	0.06	0.06	0.06
P_2O_5	0.10	0.08	0.08	0.09
ZnO	8.52	8.05	7.99	7.43
H_2O^-	0.18	<0.08	<0.08	<0.08
H_2O^+	0.82	0.27	0.29	0.33
Total	99.93	98.72	101.11	99.07

TABLE 2. Electron-microprobe analyses (oxide wt%) of unheated muscovite (Ms), muscovite pseudomorphs, and glasses around muscovite pseudomorphs.

	Quartz-feldspar glass		Unheated Ms*	Ms pseudomorph		
	10 min#	68 h#		10 min+ Core	68 h+•	68 h+• Core
SiO_2	64.6	67.8	45.6	49.1	43.5	45.8
Al_2O_3	17.7	15.5	34.3	34.3	28.8	29.8
Na_2O	3.3	3.2	0.6	3.4	2.7	3.1
K_2O	7.3	5.9	11.0	6.2	3.9	4.4
CaO	0.2	0.4	0.0	0.1	0.2	0.2
FeO-T	0.3	0.3	2.3	2.5	0.5	0.3
TiO_2	0.0	0.2	0.5	0.7	0.5	0.5
MgO	0.1	0.2	1.0	1.2	0.4	0.4
MnO	0.0	0.0	0.1	0.1	0.0	0.1
ZnO	5.2	3.6	n.a.	0.2	17.0	13.2
Total	98.7	97.1	95.4	97.8	97.5	97.8

* Average of seven analyses.
n.a.: not analysed.
+ Average of five to twenty-four "bulk" compositions (crystalline phases and glass) of muscovite pseudomorphs.
# Average of two to four analyses.
• At 68h, most pseudomorphs show a homogeneous texture, except for the largest grains (see text).

TABLE 3. TEM-EDS analyses (oxide wt%) of product phases from muscovite pseudomorphs in the heat-treated samples.

	10 min					68 h	
	Zn-rich Al-Zn spinel*	Al-rich spinel#	Willemite*	Mullite*	Glass#	Glass*	Gahnite*
SiO_2	10.2	9.3	28.7	22.3	68.1	73.1	1.3
Al_2O_3	49.0	78.4	2.8	72.3	26.7	19.7	55.4
K_2O	0.7	0.6	0.6	0.3	2.5	2.7	0.3
CaO	ND	ND	0.9	ND	ND	0.5	0.5
Fe_2O_3	5.5	2.1	1.6	2.6	0.6	0.2	2.4
TiO_2	0.3	0.1	0.7	0.4	0.3	0.7	0.8
MgO	3.1	5.1	4.5	1.9	1.4	1.3	2.5
MnO	ND	ND	0.7	ND	ND	ND	0.4
ZnO	30.8	4.4	59.6	0.0	0.4	1.8	36.4
Total	100	100	100	100	100	100	100
	Structural formula on the basis of O atoms						
	4	3	4	8			4
Si^{4+}	0.28	0.16	0.96	1.00			0.04
Al^{3+}	1.59	1.60	0.11	3.81			1.89
K^{+}	0.03	0.01	0.03	0.02			0.01
Ca^{2+}	0.00	0.00	0.03	0.00			0.02
Fe^{3+}	0.11	0.03	0.04	0.09			0.05
Ti^{4+}	0.01	0.00	0.02	0.01			0.02
Mg^{2+}	0.13	0.13	0.22	0.13			0.11
Mn^{2+}	0.00	0.00	0.02	0.00			0.01
Zn^{2+}	0.62	0.06	1.48	0.00			0.78
M^{2+}	0.75	0.19	1.76	0.13			0.91
M^{3+}	1.70	1.63	0.15	3.90			1.94
M^{4+}	0.29	0.16	0.98	1.01			0.05
$\Sigma_{cations}$	2.76	2.00	2.91	5.06			2.91

* Average of five analyses
* Average of two to six analyses
# Analysis of sixteen to twenty seven analyses.
ND: not detected